

HOKKAIDO UNIVERSITY

Title	Scaling of early afterslip velocity and possible detection of tsunami-induced subsidence by GPS measurements immediately after the 2011 Tohoku-Oki earthquake
Author(s)	Mitsui, Y.; Heki, K.
Citation	Geophysical Journal International, 195, 238-248 https://doi.org/10.1093/gji/ggt256
Issue Date	2013-06
Doc URL	https://hdl.handle.net/2115/53158
Rights	This article has been accepted for publication in Geophysical Journal International ©:The Authors 2013 Published by Oxford University Press on behalf of The Royal Astronomical Society All rights reserved.
Type	journal article
File Information	MitsuiHeki_GJI2013.pdf



Hokkaido University Collection of Scholarly and Academic Papers : HUSCAP

Geophysical Journal International

Geophys. J. Int. (2013) **195,** 238–248
Advance Access publication 2013 July 23

doi: 10.1093/gji/ggt256

Scaling of early afterslip velocity and possible detection of tsunami-induced subsidence by GPS measurements immediately after the 2011 Tohoku-Oki earthquake

Yuta Mitsui* and Kosuke Heki

Department of Natural History Sciences, Hokkaido University, Sapporo 060-0810, *Japan. E-mail: symitsu@ipc.shizuoka.ac.jp*

Accepted 2013 June 27. Received 2013 June 27; in original form 2012 September 8

SUMMARY

We explore the use of on-land GPS observations to detect deformation due to tsunami propagation near source regions of large interplate earthquakes. Here, we focus on the M_w 9 Tohoku-oki earthquake, which occurred around 14:46 (JST) on 2011 March 11. We consider GPS data in the time span 14:54–15:22 (JST) along the Sanriku coast, where the tsunami had the largest amplitude. The displacement data shows the signatures of large aftershocks as well as post-seismic fault slip (afterslip). These effects are particularly evident in the east component. From the horizontal displacement vectors, we construct a simple fault model for the early phase of the afterslip. Mean slip velocity of the early afterslip reaches 0.1 mm s^{-1}. By compiling the early afterslip velocity of recent interplate earthquakes around that region, we find its increasing trend with the main shock magnitude. This scaling relation may reflect higher stressing rates at edges of larger main shock faults. Separately, we forward calculate land deformation due to tsunami height changes based on a tsunami simulation. Tsunami-induced deformation is only evident in the vertical direction at coastal GPS stations. The predicted subsidence amounts at some coastal stations can account for a large portion of the residuals between the observation and the modelled deformation due to the fault slip.

Key words: Satellite geodesy; Transient deformation; Tsunamis; Earthquake dynamics; Subduction zone processes.

1 INTRODUCTION

Seismic slip of the 2011 Tohoku earthquake on March 11, whose moment magnitude was M_w 9, caused major deformation along the east coast of Honshu Island, Japan. A dense on-land GPS network, named GEONET, recorded the signals of the slip-induced deformation. Simons *et al.* (2011) and many other studies (e.g. Ozawa *et al.* 2011) have estimated the coseismic fault slip. Large aftershocks and afterslip were also observed by GEONET.

Land deformation associated with large interplate earthquakes is not limited to elastic displacement directly caused by interplate fault slip. For example, the Earth is strained temporarily by ocean mass movements (tsunamis) caused by fault slip, as revealed by teleseismic observations using strainmeters, broad-band seismometers and gravimeters for previous earthquakes (Yuan *et al.* 2005; Nawa *et al.* 2007; Takatsuka *et al.* 2008; Boudin *et al.* 2013; Jolly *et al.* 2013; Kimura *et al.* 2013). Such deformation could contaminate the signals of the slip-induced deformation near source faults, if displacements during the tsunami arrival are used.

Here, we estimate land deformation due to fault slip and tsunami near the source of the 2011 Tohoku earthquake. Regarding the former slip-induced deformation, early afterslip of the 2011 Tohoku earthquake had been reported by Munekane (2012). In this paper, we re-examine the amount of early afterslip at the time of the tsunami arrivals. Further, we focus on the latter tsunami-induced deformation because it's contribution to deformation field has not yet been documented for the 2011 Tohoku earthquake. We use on-land GPS data at GEONET stations along the coast line of the Sanriku, where the tsunami after the Tohoku earthquake attacked first (Hayashi *et al.* 2011) and most heavily (Mori *et al.* 2011).

Detection of tsunami-induced land deformation by satellite observations has been tried previously (Plag *et al.* 2006) but not reported. Physically, signals of tsunami-induced deformation should stand out in vertical displacement at each GPS station, since tsunami-induced land deformation is a kind of deformation by surface loads. For instance, we can simplify the problem as elastic deformation in a half-space due to a point load, the so-called Boussinesq's problem. Lamb (1902) gave the solution for the ratio of vertical displacement d_v to tangential displacement d_t at an observation point owing to a surface point load

$$\frac{d_v}{d_t} = \frac{\lambda + 2\mu}{\mu}, \tag{1}$$

*Now at: Department of Geosciences, Shizuoka University, Shizuoka 422-8529, Japan.

© The Author 2013. Published by Oxford University Press on behalf of The Royal Astronomical Society.

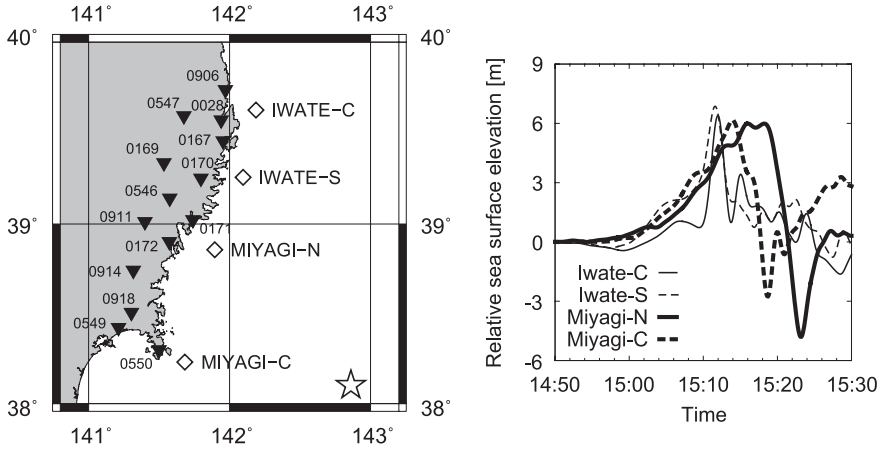


Figure 1. Left-hand: map of the Sanriku coast. The solid triangles represent the GEONET stations. We call the stations numbered 0906, 0028, 0167, 0170, 0171, 0172 and 0550 as coastal stations, and 0547, 0169, 0546, 0911, 0914, 0918 and 0549 as landward stations. One more GEONET station is located between 0172 and 0550, numbered 0036, but that station did not record the deformation signal after the Tohoku earthquake. The star indicates the epicentre of the 2011 Tohoku earthquake, determined by the Japan Meteorological Agency (142.86°E, 38.10°N). The open squares show the NOWPHAS stations to monitor sea surface height by GPS buoys. Right-hand panel: relative sea surface elevation after the 2011 Tohoku earthquake which occurred around 14:46.

where λ and μ are the first and second Lame constants in the elastic field. Noting that $(\lambda + 2\mu)/\mu \simeq 3$ for crustal materials, tsunami loading on the Earth generally causes at least three times larger vertical displacement than horizontal displacement. This characteristic contrasts with slip-induced deformation by thrust faults (e.g. Okada 1992) where the ratio is typically below one.

2 DISPLACEMENT ALONG THE SANRIKU COAST AFTER THE TOHOKU EARTHQUAKE

2.1 GEONET data

We use the 1 Hz-GPS data analysed using the precise point positioning method, provided by the Geospatial Information Authority of Japan (GSI) through Nippon GPS Data Services Company (NGDS) and the VERIPOS/APEX service using the RTNet software (GPS-Solutions). We focus on the GEONET stations located along the Sanriku coast (Fig. 1). For reference, the figure also indicates locations of NOWPHAS stations monitoring sea surface height by GPS buoys.

The 2011 Tohoku Earthquake occurred around 14:46 (JST) on March 11 and its seismic moment release continued over several minutes. The resulting massive tsunami propagated westward and attacked the Sanriku coast. Fig. 1 presents the records of the relative sea surface elevation after 14:50, at the NOWPHAS stations. As Maeda *et al.* (2011) and Fujii *et al.* (2011) reported, a tsunami with a smoothly increasing amplitude came first and a short-period impulsive tsunami followed.

The sea surface elevation data imply that the tsunami-induced subsidence along the Sanriku coast appeared by around 15:20. Therefore we focus on relative displacement at the GEONET stations during almost 30 min after the main shock. Since few coastal stations had recorded the time-series data after the tsunami arrivals, we do not try to detect the 'unloading' after the tsunami passes in this paper. Fig. 2 shows the observed horizontal and vertical displacement at the GEONET stations between the median positions at 14:54–14:56 and 15:20–15:22. All the stations moved eastward, and most of the stations subsided. We show all the time-series data in Appendix A.

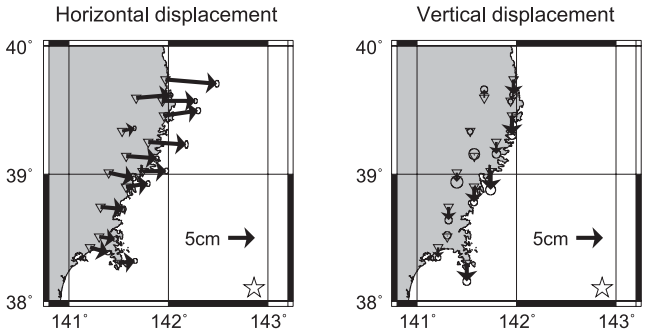


Figure 2. Observed horizontal (left-hand panel) and vertical (right-hand panel) displacement at the GEONET stations between the median positions at 14:54–14:56 and 15:20–15:22. For the horizontal displacement, diameters of each error ellipsoid are given by square sums of interquartile ranges for the time spans 14:54–14:56 and 15:20–15:22 in the east–west and north–south directions. For the vertical displacement, a diameter of each error circle is also given by square sums of interquartile ranges for the time spans 14:54–14:56 and 15:20–15:22 in the vertical direction.

2.2 Deformation by large aftershocks and afterslip

The post-seismic deformation included signals of large aftershocks and afterslip on the plate interface. In particular, the horizontal displacement at the GEONET stations should be explained by the aftershocks and afterslip.

Several large (over M_w 7) aftershocks occurred following the main shock of the 2011 Tohoku earthquake. In particular, two aftershocks, one occurred around 15:09 off Iwate (142.78°E, 39.84°N), hereafter Aftershock 1, and the other occurred around 15:16 off Ibaraki (141.27°E, 36.11°N), Aftershock 2, affected the displacement signals in Fig. 2. Fig. 3 shows simplified rectangular fault models of the main shock, Aftershock 1 and Aftershocks 2 estimated using on-land GPS data (Nishimura *et al.* 2011). We reconstruct the amounts of static displacement on the GEONET stations by Aftershocks 1 and 2 using a Green's function in a homogeneous

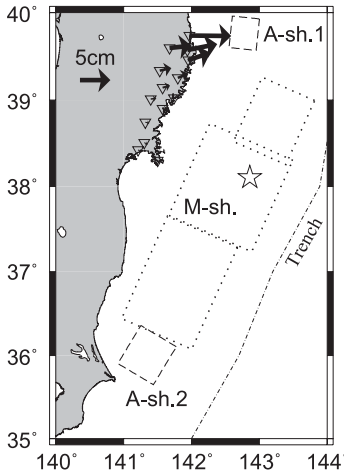


Figure 3. Rectangular fault models of the main shock, Aftershock 1, and Aftershocks 2 in the previous study (Nishimura *et al.* 2011). The main shock faults are given by the three rectangles. The GEONET stations used in this study are represented by the triangles. We also plot the reconstructed horizontal displacement due to Aftershocks 1 and 2 from the previous study. The trench line is based on DeMets *et al.* (1990).

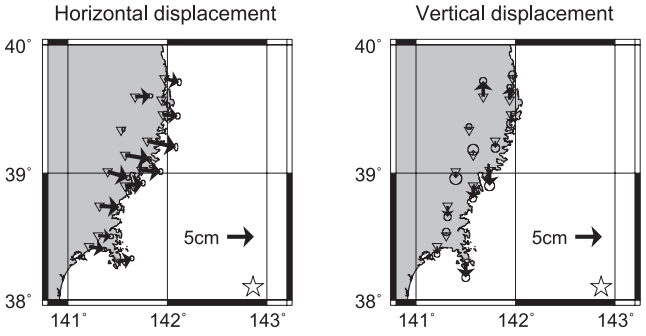


Figure 4. Residual displacement d_r between the observation (Fig. 2) and the aftershock-induced slip based on the previous study.

elastic half-space (Okada 1992), where the rigidity is assumed to be 40 GPa and the Poisson's ratio 0.25 (the same settings as Nishimura *et al.* 2011). Fig. 3 shows the calculated horizontal displacement due to Aftershocks 1 and 2. Although the aftershock model has uncertainties, we only plot the maximum likelihood solution.

The residual displacement vectors d_r between the observation and the aftershock-induced deformation are illustrated in Fig. 4. Since the horizontal displacement by tsunami load is negligible (we will confirm this point based on tsunami simulation models in a later section), we roughly estimate the early afterslip on the plate interface from the horizontal vectors during the observation period (from 14:54–14:56 to 15:20–15:22). Referring to the source faults of the main shock and Aftershock 1, and a geometry of the plate interface (e.g. Zhao *et al.* 2011; Hayes *et al.* 2012), we set two rectangular faults (x) and (y) for the afterslip as shown in Fig. 5. The afterslip faults are assumed to be separate from the source areas of the main shock and Aftershock 1. The fault parameters are given by Table 1. Slip amount of Fault (x), u_x, and that of Fault (y), u_y, are variables.

We estimate u_x and u_y simply by minimization of the residual sum of squares between the observation and the modelled deformation. First, we ignore the error ellipsoids of the observation.

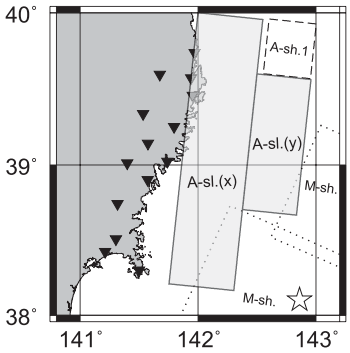


Figure 5. A fault model of the afterslip given by the two rectangulars (x) and (y) with solid lines. The afterslip faults are set to be separate from the source faults of the main shock and Aftershock 1.

Using the Green's function in a homogeneous elastic half-space (Okada 1992), we calculate displacement vectors d_c at the GEONET stations from u_x and u_y. A residual sum of squares S_1 from d_r (observation minus aftershock-induced deformation) and d_c (calculated afterslip-induced deformation) for the horizontal displacement is given by

$$S_1 = \sum_{\text{stations}} \left[(d_r - d_c)^2_{NS} + (d_r - d_c)^2_{EW} \right]. \quad (2)$$

Next, we consider the error ellipsoid of the observation at each station (Fig. 2) as weight of the residual error. We define another residual sum of squares S_1' as

$$S_1' = \sum_{\text{stations}} \left[\left(\frac{d_r - d_c}{D} \right)^2_{NS} + \left(\frac{d_r - d_c}{D} \right)^2_{EW} \right], \quad (3)$$

where D is a half width of the error ellipsoid.

Fig. 6 presents distributions of S_1 and S_1' when u_x and u_y are varied. We find that S_1 has a minimum value 2.4×10^{-3} (m^2) with $u_x = 0.18$ (m) and $u_y = 0.19$ (m) and S_1' has a least value 220 with $u_x = 0.13$ (m) and $u_y = 0.24$ (m). Fig. 7 shows the calculated horizontal displacement at each station for the least S_1 and S_1' models. The total moment magnitude is 7.2–7.3. Practically the differences in both models are negligible.

In addition, we roughly calculate the slip velocity of the afterslip based on the least S_1 model. In Fault (y), the seismic moment released from 14:54–14:56 to 15:20–15:22 was 3×10^{19} N m. Thus the mean rate of the moment release was as large as 2×10^{16} N m s^{-1}. Under the assumption of the rigidity 40 GPa, the product of slip velocity and the slip area (4×10^9 m^2), summed with the product of the slip amount and slip area change per unit time, was almost 5×10^5 m^3 s^{-1}. If we neglect propagation of the afterslip (the slip area change per unit time is zero), the slip velocity was on the order of 10^{-4} m s^{-1} = 0.1 mm s^{-1}.

2.3 Deformation by tsunami

In order to evaluate the tsunami-induced displacements, we calculate the load deformation from sea height changes in a tsunami simulation (Gusman *et al.* 2012). Namely, we obtain elastostatic deformation at the on-land GPS stations by spatially convolving sea-mass loads, which are obtained from the simulated sea-height changes during 14:55–15:21, with a Green's function. The calculation method is similar to those in several studies (Farrell 1972; Matsumoto *et al.* 2001; Plag *et al.* 2006). The tsunami-induced deformation d_{tl} at each observation point is given by

Table 1. Fault parameters for the afterslip.

Fault	Longitude[a] (°)	Latitude[a] (°)	Depth[a] (km)	Length (km)	Width (km)	Strike[b] (°)	Dip (°)	Rake[c] (°)
(x)	142.0	40.0	50.0	200.0	50.0	186.0	20.0	90.0
(y)	142.5	39.6	38.0	100.0	40.0	186.0	12.0	90.0

[a]At a northern and lower edge of rectangular fault.
[b]Rotation angle from north (clockwise).
[c]Rotation angle from the strike direction (counter-clockwise).

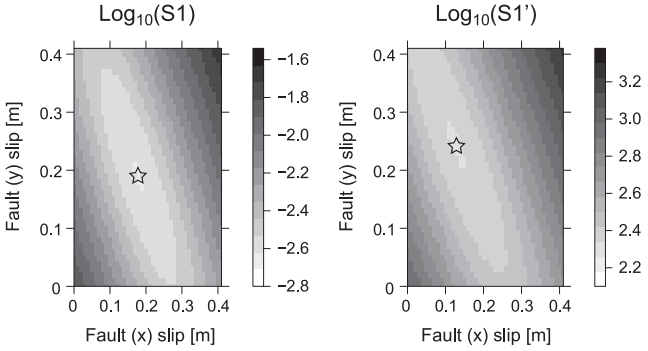


Figure 6. Distribution of the residual sum of squares S_1 and S_1' when the slip amount of Fault (x), u_x, and the slip amount of Fault (y), u_y, are varied. (Left-hand panel: S_1 has a least value 2.4×10^{-3} (m^2) with $u_x = 0.18$ (m) and $u_y = 0.19$ (m), represented by the star. Right-hand panel: S_1' has a least value 220 with $u_x = 0.13$ (m) and $u_y = 0.24$ (m), also represented by the star.

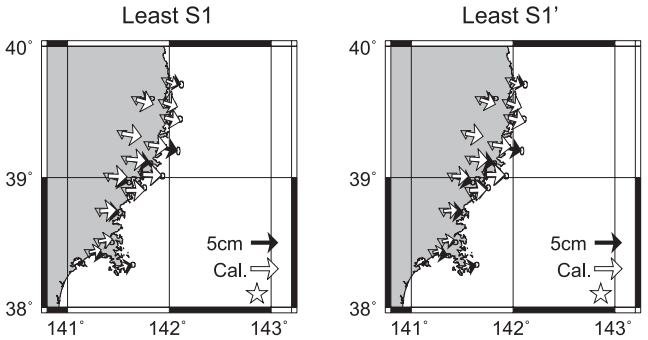


Figure 7. Calculated horizontal displacement for the least S_1 model [$u_x = 0.18$ (m) and $u_y = 0.19$ (m)] and S_1' model [$u_x = 0.13$ (m) and $u_y = 0.24$ (m)] of the afterslip, compared with the residual displacement d_r shown in Fig. 4.

$$d_{tl} = \rho A \sum_{grid} \Delta H G_f \tag{4}$$

where ρ is a water density, 1000 kg m^{-3}, A is the grid size of the tsunami simulation, $0.5' \times 0.5'$ (almost corresponding to 1 km square), and ΔH is the sea-height change at each numerical grid-point. The numerical grids are located in a range of 138°E–148°E and 34°N–42°N. G_f is a Green's function for the point load

$$G_f(\theta) = \frac{r_e}{m_e} \sum_{n=0}^{\infty} h_n P_n(\cos\theta), \tag{5}$$

where θ is an angular distance from a centre of the simulation grid to an observation point, r_e is the radius of the Earth, 6378 km; m_e is the mass of the Earth and h_n are Love numbers depending on an assumed elastic structure of the Earth, and P_n represents

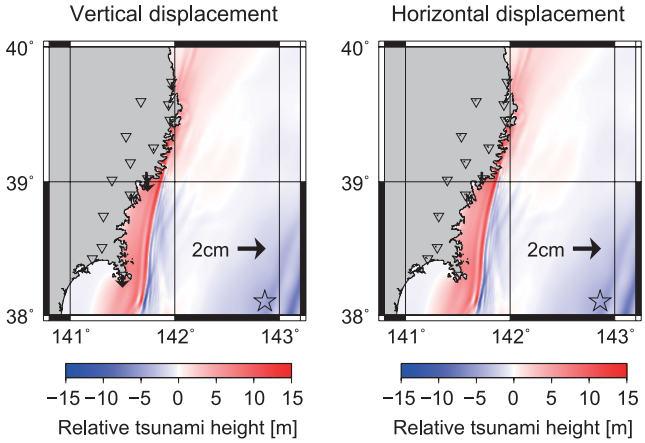


Figure 8. Calculated vertical and horizontal displacement from the simulated sea-height changes during 14:55–15:21, with the Green's function based on the PREM. The colour contour indicates the relative tsunami height from 15:21 to 14:55 in the tsunami simulation.

the Legendre function of degree n. Here, we use a Green's function (Pagiatakis 1990) based on PREM (Dziewonski & Anderson 1981).

Fig. 8 shows the simulated displacement. We find that only the coastal stations subside, by <1 cm, although the subsidence of stations 0171 and 0550 reach nearly 1 cm. By contrast, the amounts of the vertical displacement at the landward stations are too small to be detected. As we assumed in the preceding section, the horizontal displacement by the tsunami loading are too small to be detected.

3 DISCUSSION

3.1 Slip velocity of early afterslip at the Pacific Plate subduction zone

We estimated that the slip velocity of the early afterslip following the 2011 Tohoku earthquake off Sanriku was approximately as fast as 0.1 mm s^{-1} (10^{-4} m s^{-1}). Munekane (2012) also investigated the early afterslip around the same region. They estimated the slip amount was approximately 5 cm during 10 min after the main shock, which corresponds to the slip velocity of 8×10^{-5} m s^{-1}. We compare these values with other cases of recent large interplate earthquakes at the Pacific Plate subduction zone.

Fig. 9 illustrates source regions of afterslip of recent large earthquakes on the Pacific subduction plate interface. Namely we focus on the 2003 Tokachi-oki earthquake (M_w 8.3 by USGS and M_w 8.0 by JMA), the 1994 Sanriku-oki earthquake (M_w 7.7 by USGS and M_w 7.6 by JMA), the 2011 Miyagi-oki earthquake of a possible

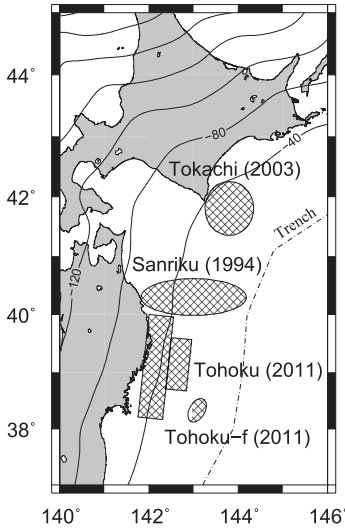


Figure 9. Source regions of afterslip of recent large earthquakes at the Pacific subduction plate interface: the 2003 Tokachi-oki earthquake (M_w 8.3 by USGS and M_w 8.0 by JMA), the 1994 Sanriku-oki earthquake (M_w 7.7 by USGS and M_w 7.6 by JMA), the 2011 Miyagi-oki earthquake of a possible foreshock for the 2011 Tohoku earthquake (M_w 7.3, written as Tohoku-f in the figure), and the 2011 Tohoku earthquake (M_w 9.0). The contours represent the depths of the plate interface (Hayes *et al.* 2012) at 40 km intervals.

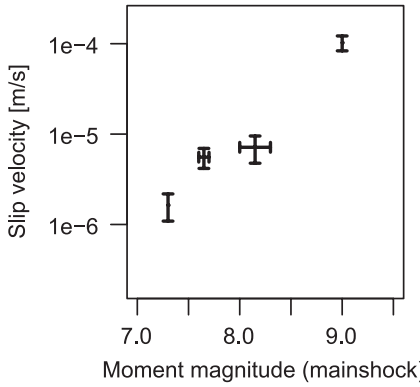


Figure 10. A compiled result for the mean slip velocity of early afterslip versus the moment magnitude of main shock at the Pacific subduction plate interface (the 2011 Tohoku earthquake of M_w 9.0; the 2003 Tokachi-oki earthquake of M_w 8.0–8.3; the 1994 Sanriku-oki earthquake of M_w 7.6–7.7, the 2011 Miyagi-oki earthquake of M_w 7.3. Note that only the result of the 2011 Miyagi-oki earthquake was based on the longer-period (almost 2 d) data than the others.

foreshock for the 2011 Tohoku earthquake (M_w 7.3, written as Tohoku-f in the figure), and the 2011 Tohoku earthquake (M_w 9.0).

We extract the slip velocity of early phases of the afterslip from previous studies. Miyazaki & Larson (2008) calculated fault slip during 70 min just after the main shock of the 2003 Tokachi-oki earthquake. The slip amount was 2–4 cm, thus the mean slip velocity was about 5×10^{-6}–1×10^{-5} m s^{-1}. Ohta *et al.* (2012) constructed an afterslip model for the 2011 Miyagi-oki earthquake. The slip amount for 51 hr (the time span between this foreshock and the main shock of the 2011 Tohoku earthquake) was 20–40 cm. Although the time span in this case was far longer than the other cases, we assessed the length effect (time decay of the afterslip) was at most two or three times, from their original time-series data. The corresponding mean slip velocity was 1×10^{-6}–2×10^{-6} m s^{-1}. In addition, we roughly estimate amount of early afterslip of the 1994 Sanriku-oki earthquake from the strainmeter data used in Heki & Tamura (1997) (Appendix B). The mean slip velocity was 4×10^{-6}–7×10^{-6} m s^{-1} (true values may be slightly larger because we did not use the oscillating time-series data immediately after the main shock). Note that acceleration of the Pacific Plate subduction after the 2003 Tokachi-oki earthquake and the 2011 Tohoku-oki earthquake (Heki & Mitsui 2013) did not affect the slip velocity of the afterslip, because the increased amounts of the plate subduction rate were the same order of magnitude as the ordinary subduction rate ($\sim 10^{-9}$ m s^{-1}).

Fig. 10 shows the compiled result for the mean slip velocity of the early afterslip versus the moment magnitude of main shock. We find that the case of the 2011 Tohoku earthquake has one order of magnitude higher slip velocity than the others. Also we find an increasing trend of the afterslip velocity for the main shock magnitude. For example, a scaling relation of $v_{af} \propto 10^{M_w}$ or $v_{af} \propto M_o^{2/3}$, where v_{af} is the slip velocity of early afterslip and M_o is the seismic moment, could be realized. The dependence is similar to the scaling relation of aftershock numbers for the main shock magnitude of interplate earthquakes in Japan (Yamanaka & Shimazaki 1990). This fact may indicate correlations of afterslip and aftershocks, for example as proposed by Matsuzawa (2004), though all of those phenomena are not necessarily occur on interplate faults.

We also note that the increasing trend of the early afterslip velocity for the main shock magnitude is different from the decreasing trend of SSE (spontaneous slow slip event) velocity for its magnitude by Meade & Loveless (2009). According to the discussion of Meade & Loveless (2009), the decreasing trend of the SSE velocity is explained by the following facts: (1) Larger SSEs have larger source areas. (2) Linear relation of seismic moment and event duration (namely, constant moment release rate) of SSE (Ide *et al.* 2007). In contrast, we confirmed non-constant moment release rate of the early afterslip by checking slip area in the above-mentioned cases as well as the slip velocity. The moment release rate of the early afterslip also increases with the increasing main shock magnitude. The increasing trend of the early afterslip is not strange, because stressing rates at edges of larger main shock faults should be higher.

The value 10^{-4} m s^{-1} in the case of the 2011 Tohoku earthquake (M9.0) implies an effective maximal velocity for afterslip phenomena. In contrast, the coseismic slip velocity of earthquakes is as fast as 10^{-1} to 10^{1} m s^{-1} (e.g. Heaton 1990; Yomogida & Nakata 1994; Yagi & Fukahata 2011). There is a gap of over 3 orders of magnitude of the slip velocity between afterslip and coseismic slip. Fig. 11 illustrates the above points.

The gap between the afterslip and seismic values may reflect properties of friction on faults. Based on rock experiments using Granite, Weeks (1993) proposed that steady-state friction turns into velocity-strengthening behaviour around 10^{-4} m s^{-1} from velocity-weakening behaviour in the lower-velocity range. This point seems consistent with our implication for the maximal afterslip velocity 10^{-4} m s^{-1}. The gap might be explained by drastic frictional weakening at very high speeds (e.g. Sibson 1973; Tsutsumi & Shimamoto 1997; Di Toro *et al.* 2011), associated with complex frictional processes, for instance, 'competition' among the change in velocity dependence of steady-state friction, porosity evolution within fault gouge, thermal fluid pressurization due to shear heating, and diffusion of heat and fluid (Mitsui & Cocco 2010).

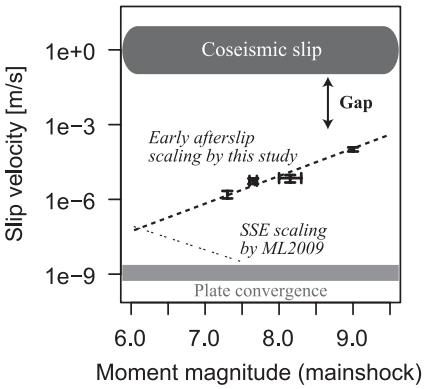


Figure 11. A schematic of the relations among velocity of the afterslip at the Pacific subduction plate interface (the same data as Fig. 10), seismic slip, and plate convergence. The gap exists between the afterslip and seismic slip over 3 orders of the slip velocity. The plotted line for the early afterslip scaling is $v_{af} \propto 10^{M_w}$ ($v_{af} \propto M_o^{2/3}$), where v_{af} is the early afterslip velocity and M_o is the seismic moment. In order to compare with the early afterslip, we also plot another scaling relation for SSE (spontaneous slow slip event) proposed by Meade & Loveless (2009) (named as ML2009 in the figure). The early afterslip is the increasing trend for the main shock magnitude, but the SSE is the decreasing trend for its magnitude.

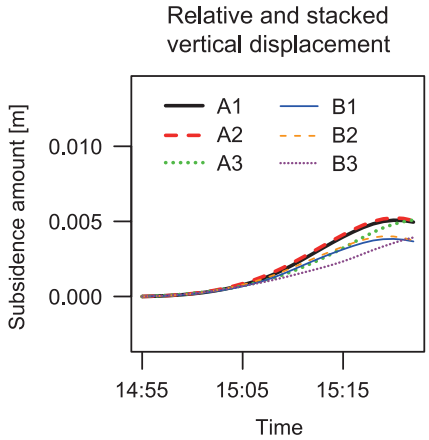


Figure 12. The simulated temporal evolution of the relative subsidence for each model: A1 (based on the Gusman *et al.* (2012) simulation with the PREM), A2 (with Gutenberg–Bullen A model), A3 (with the 1066A model), B1 (based on the Satake *et al.* (2013) simulation with the PREM), B2 (with Gutenberg-Bullen A model) and B3 (with the 1066A model). We calculate the relative subsidence by subtracting the stacked subsidence amount at the landward stations from that at the coastal stations.

3.2 Examination of vertical deformation amount due to tsunami load

In the previous Section 2.3, we simulated that only the coastal stations subsided by subcentimetre due to sea-mass loads based on the tsunami simulation (Gusman *et al.* 2012). The subsidence amounts of stations 0171 and 0550 reached almost 1 cm. The amounts are not negligible but still not sufficiently large values to be detected by GPS robustly. Here we further examine the amounts of the tsunami-induced subsidence.

First, we investigate effects of the assumed velocity structure to calculate the surface-load deformation. All of the above calculations were based on the PREM (Dziewonski & Anderson 1981). As an alternative velocity structure model, we try two earth structure models: the Gutenberg–Bullen A model (Alterman *et al.* 1961) and the 1066A model [Gilbert & Dziewonski (1975), where the Green's function was given by Okubo & Saito (1983) and Endo & Okubo (1984)]. We call three models as A1, A2 and A3, respectively. Moreover, we test another tsunami simulation model (Satake *et al.* 2013) as a source of the surface loads. We also name three models with the different earth structure models as B1, B2 and B3. In order to compare the six models, we calculate relative subsidence amounts of the coastal stations (0906, 0028, 0167, 0170, 0171, 0172 and 0550) from the landward stations (0547, 0169, 0546, 0911, 0914, 0918 and 0549). We stack the simulated values for the coastal stations and the landward stations, respectively, to take their difference. Fig. 12 shows the temporal evolution in the relative subsidence for each model. We find that the model uncertainties do not alter the calculation results so much.

Second, we speculate that permanent seafloor deformation owing the main shock (Tsushima *et al.* 2012) caused non-negligible subsidence, via permanent sea-mass movement above the deformed seafloor. Here we call this deformation as 'secondary' vertical displacement, where 'primary' vertical displacement is directly caused by the main shock fault slip. Our previous calculations were based on the tsunami simulations of which initial conditions were sea-height changes due to the primary displacement, thus they did not consider the permanent sea-mass movement and the secondary displacement. In order to estimate the amount of the secondary vertical displacement, we check the primary vertical displacement in the 2011 Tohoku earthquake. For example, Simons *et al.* (2011) revealed that the primary vertical displacement near the Sanriku coast was as large as several metres subsidence. This coseismic subsidence led to permanent sea-mass increases above the region. By a rough calculation using the boundary element method (Farrell 1972) with the Green's function (Pagiatakis 1990), we find that the subsidence amount of the secondary vertical displacement along the Sanriku coast reached several millimetres, a little less than the previously simulated subsidence amount. This fact implies: (1) the total amount of the tsunami-induced subsidence could be twice the amount of the calculated values from the tsunami simulation, since the permanent sea-mass movement do not occur immediately after the main shock. (2) the tsunami-induced subsidence does not necessarily vanish after the finish of the tsunami phenomenon (transient wave).

Of course, for more quantitative discussion, we should consider other factors such as dynamic loading effects (e.g. Okubo & Tsuji 2001), meridian changes at the observation points, or size effects of the simulation grids near the coast. Moreover, water inundation and run-up inland to several kilometres (Mori *et al.* 2011), which were not implemented in the referred simulation, would increase the subsidence amounts at the GPS stations.

3.3 Possibility of detection of tsunami-induced subsidence

As was discussed above, we expected that the vertical displacement due to the tsunami-loading was at most 1 cm or more, at coastal stations 0550 and 0171. We consider the possibility of the detection of the tsunami-induced subsidence at these two stations.

Fig. 13 shows comparative results between the observed subsidence (Fig. 2) and modelled subsidence due to the aftershocks, afterslip and tsunami at stations 0550 and 0171. The model of the

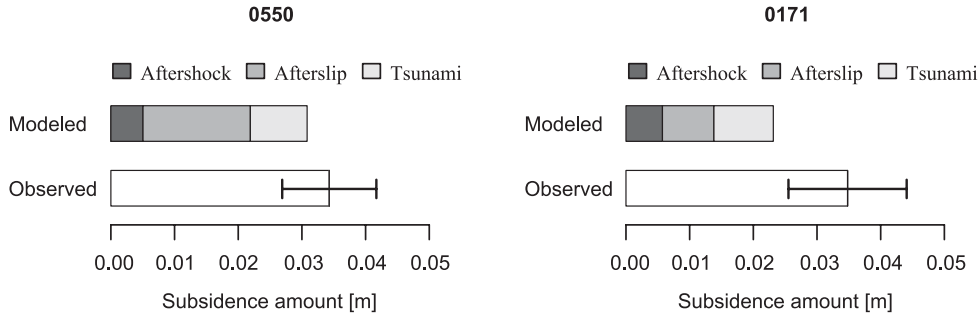


Figure 13. Comparative results between the observed subsidence with the error bars (Fig. 2) and modelled subsidence due to the aftershocks, afterslip and tsunami at coastal stations 0550 and 0171. The model of the afterslip deformation is the least S_1 model, and the tsunami deformation is model A1.

afterslip deformation is the least S_1 model, and the tsunami deformation is model A1.

We find that the tsunami-induced subsidence might reach tens of percent of the observed subsidence amounts at the two coastal stations. The predicted subsidence amounts account for a large portion of the residuals between the observation and the modelled deformation due to the fault slip. On the other hand, model uncertainties of the fault slip phenomena (aftershocks and afterslip) could exceed the tsunami-induced signals. It means that further discussion is difficult without detailed models of the fault slip phenomena in this condition.

4 CONCLUSION

We checked the on-land GPS data along the Sanriku coast during almost 30 min after the M_w 9 Tohoku earthquake, where the tsunami had the largest amplitude. The M_w 7-class aftershocks, the afterslip and the tsunami caused land deformation, respectively. First, we modelled the early phase of the afterslip. The mean slip velocity of the early afterslip reached 0.1 mm s^{-1}. This value is one-order larger than the early afterslip of the recent large earthquakes at the Pacific subduction plate interface. We found that the early afterslip velocity v_{af} had the increasing trend with the main shock magnitude. This analysis implied $v_{af} \propto M_o^{2/3}$ (M_o is the seismic moment of the main shock). Next, we calculated the tsunami-induced deformation based on the tsunami simulation models. The expected subsidence amounts at some coastal stations were as large as 1 cm, which can explain a large part of the gaps between the observation and the modelled slip-induced deformation.

ACKNOWLEDGEMENTS

We are grateful to Saskia Goes, Jeff Freymueller, and an anonymous reviewer for editorial jobs and reviews. We thank Aditya Gusman, Yuichiro Tanioka and Yushiro Fujii for providing us their simulation results. Comments and discussion with Yusaku Ohta, Takeshi Kimura, Kazunari Nawa and Koji Matsuo improved this manuscript. We also appreciate GSI, NGDS and the VERIPOS/APEX service using the RTNet software (GPS-Solutions) for providing the GPS data (GEONET). The GPS buoy data (NOWPHAS) maintained by Ministry of Land, Infrastructure, Transport and Tourism were provided by Port and Airport Research Institute. We use Generic Mapping Tools (Wessel & Smith 1995) to draw figures.

REFERENCES

Alterman, Z., Jarosch, H. & Pekeris, C.L., 1961. Propagation of Rayleigh waves in the Earth, *Geophys. J. Int.,* **4,** 219–241.

Boudin, F. *et al.*, 2013. Analysis and modelling of tsunami-induced tilt for the 2007, M = 7.6, Tocopilla and the 2010, M = 8.8 Maule earthquakes, Chile, from long-base tiltmeter and broadband seismometer records, *Geophys. J. Int.,* **194,** 269–288.

DeMets, C., Gordon, R.G., Argus, D.F. & Stein, S., 1990. Current plate motions, *Geophys. J. Int.,* **101,** 425–478.

Di Toro, G. *et al.*, 2011. Fault lubrication during earthquakes, *Nature,* **471,** 494–498.

Dziewonski, A.M. & Anderson, D.L., 1981. Preliminary reference Earth model, *Phys. Earth planet. Int.,* **25,** 297–356.

Endo, T. & Okubo, S., 1984. A correction to 'Partial derivative of Love numbers', *Bull. Geod.,* **58,** 73–74.

Farrell, W.E., 1972. Deformation of the Earth by surface loads, *Rev. Geophys.,* **10,** 761–797.

Fujii, Y., Satake, K., Sakai, S., Shinohara, M. & Kanazawa, T., 2011. Tsunami source of the 2011 off the Pacific coast of Tohoku, Japan earthquake, *Earth Planets Space,* **63,** 815–820.

Gilbert, F. & Dziewonski, A.M., 1975. An application of normal mode theory to the retrieval of structural parameters and source mechanisms from seismic spectra, *Phil. Trans. R. Soc. Lond. A,* **278,** 187–269.

Gusman, A.R., Tanioka, Y., Sakai, S. & Tsushima, H., 2012. Source model of the great 2011 Tohoku earthquake estimated from tsunami waveforms and crustal deformation data, *Earth planet. Sci. Lett.,* **341–344,** 234–242.

Hayashi, Y., Tsushima, H., Hirata, K., Kimura, K. & Maeda, K., 2011. Tsunami source area of the 2011 off the Pacific coast of Tohoku Earthquake determined from tsunami arrival times at offshore observation stations, *Earth Planets Space,* **63,** 809–813.

Hayes, G., Wald, D. & Johnson, R., 2012. Slab1.0: a three-dimensional model of global subduction zone geometries, *J. geophys. Res.,* **117,** doi:10.1029/2011JB008524.

Heaton, T., 1990. Evidence for and implications of self-healing pulses of slip in earthquake rupture, *Phys. Earth planet. Int.,* **64,** 1–20.

Heki, K., Miyazaki, S. & Tsuji, H., 1997. Silent fault slip following an interplate thrust earthquake at the Japan Trench, *Nature,* **386,** 595–598.

Heki, K. & Mitsui, Y., 2013. Accelerated pacific plate subduction following interplate thrust earthquakes at the Japan trench, *Earth planet. Sci. Lett.,* **363,** 44–49.

Heki, K. & Tamura, Y., 1997. Short term afterslip in the 1994 Sanriku-Haruka-Oki earthquake, *Geophys. Res. Lett.,* **24,** 3285–3288.

Ide, S., Beroza, G.C., Shelly, D.R. & Uchide, T., 2007. A scaling law for slow earthquakes, *Nature,* **447,** 76–79.

Jolly, A.D., Power, W., Fournier, N. & Wang, X., 2013. Capturing transient mass changes for the 2011 Tohoku Tsunami on a spring gravity meter, *Bull. seism. Soc. Am.,* **103,** 1622–1627.

Kimura, T., Tanaka, S. & Saito, T., 2013. Ground tilt changes in whole Japan caused by the 2010 Maule, Chile, earthquake tsunami, *J. geophys. Res.,* **118,** 406–415.

Lamb, H., 1902. On Boussinesq's problem, *Proc. Lond Math Soc.,* **34,** 276–284.

Maeda, T., Furumura, T., Sakai, S. & Shinohara, M., 2011. Significant tsunami observed at ocean-bottom pressure gauges during the 2011 off the Pacific coast of Tohoku Earthquake, *Earth Planets Space,* **63,** 803–808.

Matsumoto, K., Sato, T., Takanezawa, T. & Ooe, M., 2001. GOTIC2: a program for computation of oceanic tidal loading effect, *J. Geod. soc. Japan,* **47,** 243–248.

Matsuzawa, T., Uchida, N., Igarashi, T., Okada, T. & Hasegawa, A., 2004, Repeating earthquakes and quasi-static slip on the plate boundary east off northern Honshu, Japan, *Earth Planets Space,* **56,** 803–811.

Meade, B.J. & Loveless, J.P., 2009. Predicting the geodetic signature of $M_w >$ 8 slow slip events, *Geophys. Res. Lett.,* **36,** doi:10.1029/2008GL036364.

Mitsui, Y. & Cocco, M., 2010. The role of porosity evolution and fluid flow in frictional instabilities: a parametric study using a spring-slider dynamic system, *Geophys. Res. Lett.,* **37,** doi:10.1029/2010GL045672.

Miyazaki, S. & Larson, K., 2008. Coseismic and early postseismic slip for the 2003 Tokachi-oki earthquake sequence inferred from GPS data, *Geophys. Res. Lett.,* **35,** doi:10.1029/2007GL032309.

Mori, N., Takahashi, T., Yasuda, T. & Yanagisawa, H., 2011. Survey of 2011 Tohoku earthquake tsunami inundation and run-up, *Geophys. Res. Lett.,* **38,** doi:10.1029/2011GL049210.

Munekane, H., 2012. Coseismic and early postseismic slips associated with the 2011 off the Pacific coast of Tohoku Earthquake sequence: EOF analysis of GPS kinematic time series, *Earth Planets Space,* **64,** 1077–1091.

Nawa, K., Suda, N., Satake, K., Fujii, Y., Sato, T., Doi, K., Kanao, M. & Shibuya, K., 2007. Loading and Gravitational Effects of the 2004 Indian Ocean Tsunami at Syowa Station, Antarctica, *Bull. seism. Soc. Am.,* **97,** 271–278.

Nishimura, T., Munekane, H. & Yarai, H., 2011. The 2011 off the Pacific coast of Tohoku Earthquake and its aftershocks observed by GEONET, *Earth Planets Space,* **63,** 631–636.

Ohta, Y. *et al.*, 2012. Geodetic constraints on afterslip characteristics following the March 9, 2011. Sanriku-oki earthquake, Japan, *Geophys. Res. Lett.,* **39,** doi:10.1029/2012GL052430.

Okada, Y., 1992. Internal deformation due to shear and tensile faults in a half-space, *Bull. seism. Soc. Am.,* **82**(2), 1018–1040.

Okubo, S. & Saito, M., 1983. Partial derivative of Love numbers, *Bull. Geod.,* **57,** 167–179.

Okubo, S. & Tsuji, D., 2001. Complex Green's Function for Diurnal/Semidiurnal Loading Problems, *J. Geod. Soc. Jpn.,* **47,** 225–230.

Ozawa, S., Nishimura, T., Suito, H., Kobayashi, T., Tobita, M. & Imakiire, T., 2011. Coseismic and postseismic slip of the 2011 magnitude-9 Tohoku-Oki earthquake, *Nature,* **475,** 373–377.

Pagiatakis, S.D., 1990. The response of a realistic Earth to ocean tide loading, *Geophys. J. Int.,* **103,** 541–560.

Plag, H.-P., Blewitt, G., Kreemer, C. & Hammond, W.C., 2006. Solid Earth deformations induced by the Sumatra earthquakes of 2004–2005: GPS detection of co-seismic displacements and tsunami-induced loading, in *Dynamic Planet—Monitoring and Understanding a Dynamic Planet with Geodetic and Oceanographic Tools (International Association of Geodesy Symposia),* Vol. 130, pp. 549–556, eds Tregoning, P. & Rizos, C., Springer Verlag.

Satake, K., Fujii, Y., Harada, T. & Namegaya, Y., 2013. Time and space distribution of coseismic slip of the 2011 Tohoku Earthquake as inferred from tsunami waveform data, *Bull. seism. Soc. Am.,* **103,** 1473–1492.

Sibson, R.H., 1973. Interactions between temperature and fluid pressure during earthquake faulting—a mechanism for partial or total stress relief, *Nature,* **243,** 66–68.

Simons, M. *et al.*, 2011. The 2011 Magnitude 9.0 Tohoku-Oki Earthquake: Mosaicking the megathrust from seconds to centuries, *Science,* **332,** 1421–1425.

Takatsuka, K., Ohta, Y., Miura, S., Sato, T. & Fujii, Y., 2008. Surface deformation caused by the 2004 Indian Ocean Tsunami observed at Diego Garcia, *EOS, Trans. Am. geophys. Un.,* **89,** 1330.

Tsushima, H., Hino, R., Tanioka, Y., Imamura, F. & Fujimoto, H., 2012. Tsunami waveform inversion incorporating permanent seafloor deformation and its application to tsunami forecasting, *J. geophys. Res.,* **117,** doi:10.1029/2011JB008877.

Tsutsumi, A. & Shimamoto, T., 1997. High-velocity frictional properties of gabbro, *Geophys. Res. Lett.,* **24,** 699–702.

Weeks, J., 1993. Constitutive laws for high-velocity frictional sliding and their influence on stress drop during unstable slip, *J. geophys. Res.,* **98,** 17 637–17 648.

Wessel, P. & Smith, W.H.F., 1995. New version of the generic mapping tools released, *EOS, Trans. Am. geophys. Un.,* **76,** 329.

Yagi, Y. & Fukahata, Y., 2011. Rupture process of the 2011 Tohoku-oki earthquake and absolute elastic strain release, *Geophys. Res. Lett.,* **38,** doi:10.1029/2011GL048701.

Yamanaka, Y. & Shimazaki, K., 1990. Scaling relationship between the number of aftershocks and the size of the main shock, *J. Phys. Earth,* **38,** 305–324.

Yomogida, K. & Nakata, T., 1994. Large slip velocity of the surface rupture associated with the 1990 Luzon earthquake, *Geophys. Res. Lett.,* **21,** 1799–1802.

Yuan, X., Kind, R. & Pedersen, H.A., 2005. Seismic monitoring of the Indian Ocean tsunami, *Geophys. Res. Lett.,* **32,** doi:10.1029/2005GL023464.

Zhao, D., Huang, Z., Umino, N., Hasegawa, A. & Kanamori, H., 2011. Structural heterogeneity in the megathrust zone and mechanism of the 2011 Tohoku-oki earthquake (M_w 9.0), *Geophys. Res. Lett.,* **38,** L17308, doi:10.1029/2011GL048408.

APPENDIX A: GPS TIME-SERIES DATA AFTER THE 2011 TOHOKU EARTHQUAKE

Figs A1 and A2 show the relative displacement at the coastal and landward GEONET stations from 14:54, on 2011 March 11, in the east–west (E–W), north–south (N–S), and vertical directions.

APPENDIX B: EARLY AFTERSLIP OF THE 1994 SANRIKU-OKI EARTHQUAKE

We estimate the slip amount of early afterslip in the case of the 1994 Sanriku-oki earthquake. We use an extensometer at the Esashi Earth Tide Station (EETS, 141.34°E, 39.15°N) near the source area. The extensometer provided strain data every 10 min with less noise than GPS at that time, which is useful to investigate the early afterslip (Heki & Tamura 1997). Fig. B1 shows the location of the station and the afterslip fault model by Heki *et al.* (1997).

We focus on the early phase of the afterslip during 2 hr starting almost 1 hr after the main shock (because the time-series data immediately after the main shock oscillated). Fig. B1 also presents the time-series data in three horizontal components (north–south, east–west, and northern east–southern west). Using the Green's function in a homogeneous elastic half-space (Okada 1992) and the afterslip model by Heki *et al.* (1997), we find that dislocation of 3–5 cm at the model faults explain the data. The corresponding mean slip velocity is 4×10^{-6} to 7×10^{-6} m s^{-1}.

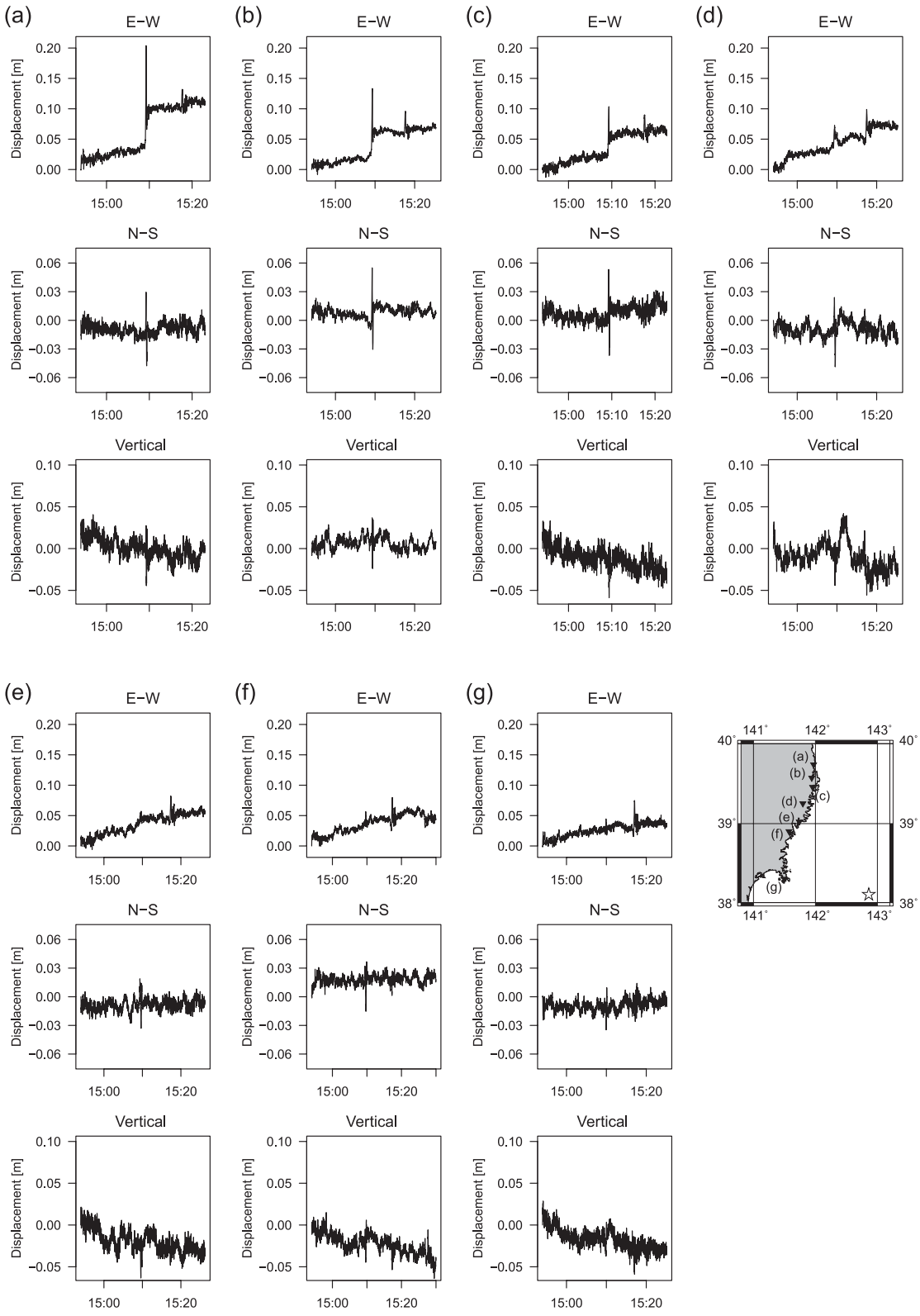


Figure A1. Three-direction relative displacement at the coastal stations: (a) at 0906 station; (b) at 0028 station; (c) at 0167 station; (d) at 0170 station; (e) at 0171 station; (f) at 0172 station and (g) at 0550 station. Most of the time-series data did not continue up to 15:30, owing to electric outages by tsunami arrivals. Only the data at 0172 station remained. The lowest right-hand panel illustrates the station locations.

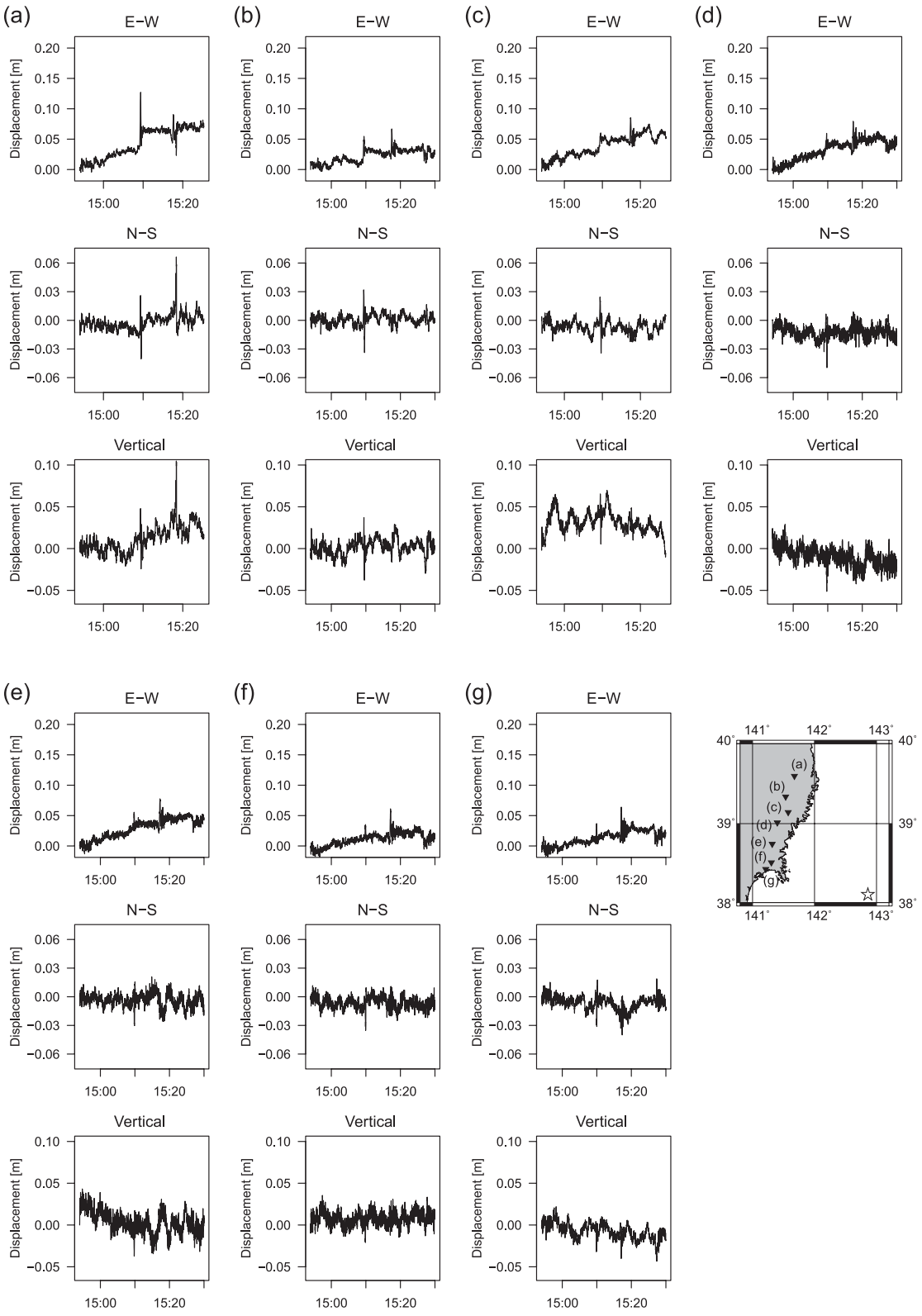


Figure A2. Three-direction relative displacement at the landward stations: (a) at 0547 station; (b) at 0169 station; (c) at 0546 station; (d) at 0911 station; (e) at 0914 station; (f) at 0918 station and (g) at 0549 station. The time-series data at 0546 and 0547 stations were not continuous up to 15:30. The lowest right-hand panel illustrates the station locations.

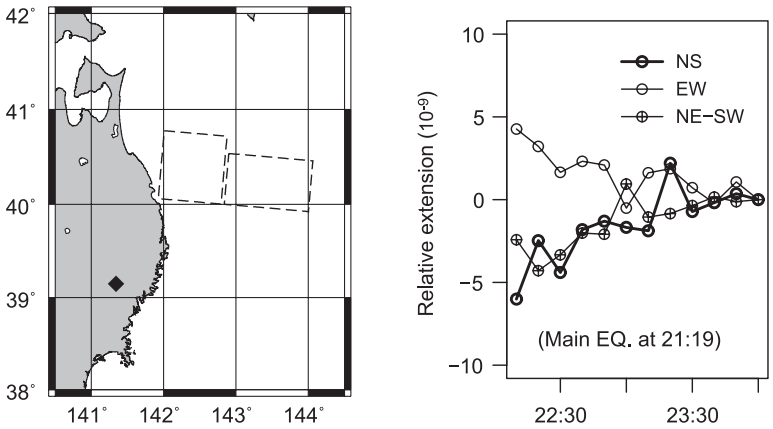


Figure B1. Left-hand panel: the location of the extensometer at EETS station represented by the solid rhombus, and the fault model of the afterslip by Heki *et al.* (1997). Right-hand panel: the extensometer data during 2 hr from almost 1 hr after the main shock. The relative extension in each component means the relative values from those at 24:00. The time zone is JST.